Sampling of finite elements for sparse recovery in large scale 3D electrical impedance tomography

Ashkan Javaherian[1], Manuchehr Soleimani[2] and Knut Moeller[1]

[1]Institute of Technical Medicine, Faculty of Medical and Life Sciences, Furtwangen University of Applied Sciences, VS-Schwenningen, Germany

[2]Engineering Tomography Laboratory (ETL), Department of Electrical Engineering, University of Bath, Bath, UK

E-mail: m.soleimani@bath.ac.uk

Abstract

This study proposes a method to improve performance of sparse recovery inverse solvers in three-dimensional electrical impedance tomography (3D EIT), especially when volume under study contains small-sized inclusions, e.g., 3D imaging of breast tumours. Initially, a quadratic regularized inverse solver is applied in a fast manner with a stopping threshold much greater than the optimum. Based on assuming a fixed level of sparsity for the conductivity field, finite elements are then sampled via applying a compressive sensing (CS) algorithm to the rough blurred estimation previously done by the quadratic solver. Finally, a sparse inverse solver is applied solely to the sampled finite elements, with the solution to the CS as its initial guess. The results show the great potentials of the proposed CS-based sparse recovery in improving accuracy of sparse solution to the large-size 3D EIT.

Keywords: electrical impedance tomography, large-size 3D, sparse recovery, finite element sampling, compressive sensing

1. Introduction

As an imaging modality emerging in field of medical diagnosis, electrical impedance tomography (EIT) seeks to calculate a map of conductivity field inside human body organs. This is done via successively injecting an electrical current through some electrodes attached to the surface of the medium and reading the induced voltages on the remaining surface electrodes (Cheney *et al* 1999). By employing finite element method, a discrete approximation of partial information over the domain, the so-called

Neumann-to-Dirichlet (NtD) map, is calculated (Holder 2005). Typically, image reconstruction in EIT involves forward and inverse problems, the first of which is to calculate electrical potential distribution over the domain based on the NtD map and the second is to update the conductivity field by minimizing ℓ_2 norm of discrepancy between the computed and the real measured voltages on the electrodes, namely residual function (Yorkey *et al* 1987, Lionheart 2004). To combat instability of such minimization problem, a regularization penalty, which usually exploits *a priori* assumption around the solution, is added to the residual function. Classical quadratic (ℓ_2) penalty have been of interest from the inaugural work in EIT (Cheney *et al* 1990, Adler and Guardo1996, Javaherian *et al* 2013). Recently, sparse regularization has shown its great potentials in recovering conductivity fields having a sparse representation (Gehre *et al* 2012, Jin *et al* 2012). Total Variation (TV) regularization can also be regarded as a class of sparse regularization with the capability of preserving sharp variations over piecewise conductivity fields (Dobson and Santosa 1994, Borsic *et al* 2010).

Since electrical current cannot stay solely aligning the electrodes plane, and inherently spreads out in three dimensions, 3D EIT has provoked much attention (Gobel *et al* 1992, Metherall *et al* 1996, Vauhkonen *et al* 1999, Halter *et al* 2007, Goharian *et al* 2009, Javaherian and Soleimani 2013). It, however, suffers from the need for a large number of finite elements for the inverse mesh, which makes the inverse problem severely ill-posed (Blue *et al* 2000, Yang *et al* 2013). To mitigate the ill-posedness of 3D EIT, numerous methods have been put forward. One way is to employ Nodal Jacobian inverse solver, which treats nodal points over the mesh rather than the finite elements (Graham and Adler 2006).

The objective of this work is to improve sparse recovery for large-size 3D EIT. It will be shown that the standard application of sparse recovery algorithms to large-size 3D EIT fails to yield an accurate solution. Indeed, the ratio of data size to the number of the unknown parameters is much low in such cases, leading to a severely ill-posed problem. In light of the fact that convergence of gradient based recovery algorithms specifically depend on the number of the sought parameters and the starting point, an approach to deal with large-size 3D EIT is proposed. A classical quadratic regularized solver is first employed in a fast manner with a stopping threshold 50-100 times greater than the optimum. The quadratic solver that is usually employed in 3D EIT is

the preconditioned conjugate gradient (PCG), thanks to its ability to solve the problem without the need for the costly calculation of inverse Hessian (Polydorides *et al* 2002). The finite elements are then sampled via application of a compressive sensing (CS) scheme to the erroneous solution already calculated by the PCG. Generally, the CS states that a random projection of a sparse signal preserves most of its salient information under some certain conditions (Candès and Tao 2005, Baraniuk 2007, Baraniuk 2010). Inspired by this theory, the fast estimation already done through the PCG is assumed as a random projection of an unknown sparse conductivity field with a fixed level of sparsity (K). The K-sparse solution is now calculated from this random projection based on the CS theory. K must be chosen so that it represents a maximum level of sparsity for the conductivity field.

The sparse recovery is then applied solely to the K sampled finite elements with the CS solution as the initial guess. The conductivity over the remaining elements is set to background. The proposed scheme is applied to the most efficient sparse recovery codes, i.e., sparse reconstruction by separable approximation (SpaRSA) (Wright *et al* 2009), Gradient projection for sparse reconstruction (GPSR) (Figueiredo *et al* 2007) and TVAL3 (Li 2009). The results show that the CS scheme appreciably improved the accuracy of the ℓ_1 recovery codes, while preserving the computational time.

2. Theory

2.1. Forward and inverse models

The forward problem in EIT is to calculate the voltages on the electrodes ($\mathbf{V}$) as responses to the injected currents and as a function of the conductivity field ($\boldsymbol{\sigma}$). Since the NtD map is a nonlinear function of the conductivity field, the forward operator is linearized around an arbitrary conductivity via computing the Jacobian ($\mathbf{J}$) (Lionheart 2004).

It turns out that time difference reconstruction, which deals with conductivity changes between two different times, suitably combats errors during the measurement (Barber and Brown 1998). In light of the linearization and the time difference reconstruction, the forward model yields the linear system $\delta\mathbf{V} = \mathbf{J}\delta\boldsymbol{\sigma}$. The inverse problem is now to calculate $\delta\boldsymbol{\sigma}$ from $\delta\mathbf{V}$ as follows.

$$\arg\min_{\delta\boldsymbol{\sigma}} \left\| \mathbf{J}\delta\boldsymbol{\sigma} - \delta\mathbf{V} \right\|_2^2 \quad \text{s.t.} \quad \textit{a priori} \text{ on } \delta\sigma \tag{1}$$

In the unconstrained form of the problem, the *a priori* is added to the residual function in the form

$$\arg\min_{\check{\mathbf{u}}\mathring{\mathbf{u}}} \frac{1}{2}\left\|\mathbf{J}\check{\mathbf{u}}\mathring{\mathbf{u}} - \check{\mathbf{u}}\mathbf{V}\right\|_2 + \lambda R_r(\check{\mathbf{u}}\mathring{\mathbf{u}}), \tag{2}$$

$$\text{where } R_r(\vartheta) = \frac{1}{r}\left\|\vartheta\right\|_{l_r}^{r}. \tag{3}$$

The choice of $r = 2$ conducts the problem to the classical quadratic form, whereas $r = 1$ yields the sparse recovery.

2.2. Preconditioned conjugate gradient (PCG)

Employing classical Newtonôs methods for solving the quadratic regularized solvers typically requires the inverse Hessian, and therefore, does not suit the large-size 3D EIT. To deal with the large number of the unknown parameters in such cases, conjugate gradient methods are often employed. In the first stage of the proposed scheme, the PCG solver was run with a terminating threshold 50-100 times greater than the optimum. The PCG solver is available on the EIDORS website (http://eidors3d.sourceforge.net). For further information on the PCG, the reader is referred to Shewchuk (1994) or Polydorides *et al* (2002). Note that the PCG is not applied here to reconstruct the final image, but only provides a fast rough estimate of the conductivity field.

2.3. Compressed sampling (CS)

It turns out that signal $\mathbf{x} \in R^N$ can be represented as a sparse signal over basis expansion $\mathbf{x} = \boldsymbol{\gamma}\mathbf{U}$, with $\boldsymbol{\gamma} \in R^{N\times N}$ projecting the basis coefficients $\mathbf{U}$ to $\mathbf{x}$. Generally, *K*-sparsity of $\mathbf{U}$ over basis $\boldsymbol{\gamma}$ implies that only K of N coefficients of $\mathbf{U}$ are nonzero. Compressed sampling (CS) states that a signal with a *K*-sparsity over basis $\boldsymbol{\gamma}$ can be recovered from noisy measurement $\mathbf{y} = \acute{\mathbf{u}}\mathbf{x}$ under the condition that $\acute{\mathbf{u}}$ satisfies so-called restricted isometry property (RIP) (Candès and Tao 2005, Donoho 2006, Baraniuk 2007, Baraniuk 2010).

In a similar way, assuming a *K*-sparsity for the unknown conductivity field $\check{\mathbf{u}}\mathring{\mathbf{u}}$, the objective is to extract K finite elements involving the salient information of $\check{\mathbf{u}}\mathring{\mathbf{u}}$ from the noisy measurement $\mathbf{y}$, where $\mathbf{y}$ is assumed to be the rough estimation already done by the PCG.

Theoretically, the *K*-sparse signal $\mathbf{x}$ can be exactly calculated from the compressive measurement $\mathbf{y} = \acute{\mathbf{u}}\mathbf{x} \in R^M$ $(M \le N)$, if $\acute{\mathbf{u}}$ satisfies the *K*-RIP, i.e.,

$$(1-\delta_K)\|\mathbf{x}\|_2^2 \le \|\mathbf{\acute{u}}\mathbf{x}\|_2^2 \le (1+\delta_K)\|\mathbf{x}\|_2^2, \quad (4)$$

where δ_K is a small scalar value.

2.3.1. Application of structure to the K-sparse signal

Let *K*-sparse signal $\mathbf{x}$ resides in $\Sigma_K \subset R^N$, where Σ_K denotes a union of all possible $\binom{N}{K}$ subspaces of dimension *K*, and let support of $\mathbf{x}$ is the set of indices pertaining to nonzero entries of $\mathbf{x}$.

Here we adopt a model-based compressive sensing scheme, the so-called CoSaMP (Model-based Compressive Sensing Toolbox v1.1). Typically, the structure considers additional features other than the sparsity, thus reducing the number of possible *K*-sparse signals living in Σ_K. By denoting entries of signal $\mathbf{x}$ that pertain to the set of indices $\Omega \subseteq \{1,,...,N\}$ by $x|_\Omega$ and also denoting the complement of the set ϙ by Ω^C, *union-of-subspace signal model* $M_K \subseteq \Sigma_K$ is defined as the union of all possible $m_K \le \binom{N}{K}$ subspaces of dimension *K* in the form

$$M_K = \bigcup_{m=1}^{m_K} \chi_m, \quad \text{s.t.} \quad \chi_m := \{\mathbf{x} : \mathbf{x}|_{\Omega_m} \in R^K, \mathbf{x}|_{\Omega_m^C} = 0\}. \quad (5)$$

Where, $\{\Omega_1,...,\Omega_{m_K}\}$ is the set of all supports satisfying $|ϙ_m| = K$ for each $m = 1,..., m_K$, χ_m is the subspace containing all signals $\mathbf{x}$ with $\text{supp}(x) \subseteq ϙ_m$, and $M_K \subseteq \sum_K$ is the union of m_K subspaces χ_m (Baraniuk 2007, Baraniuk 2010). Matrix $\mathbf{\acute{u}} \in R^{M\times N}$ satisfies M_K-RIP with constant δ_{M_K}, if for all $\mathbf{x} \in M_K$,

$$(1-\delta_{M_K})\|\mathbf{x}\|_2^2 \le \|\mathbf{\acute{u}}\mathbf{x}\|_2^2 \le (1+\delta_{M_K})\|\mathbf{x}\|_2^2. \quad (6)$$

The most accurate *K*-structured sparse approximation of $\mathbf{x} \in R^N$ over the union of subspaces M_K is given by

$$M(\mathbf{x}, K) = \arg\min_{\bar{\mathbf{x}} \in M_K} \|\mathbf{x} - \bar{\mathbf{x}}\|_2. \quad (7)$$

The B-order sum for the structured sparse signals residing in the union of subspaces M_K is defined as

$$M_K^B = \{\mathbf{x} = \sum_{r=1}^{B} \mathbf{x}^{(r)}, \quad \mathbf{x}^{(r)} \in M_K\}, \quad (8)$$

where $B > 1$ is an integer value, and $r > 0$ is the regularity parameter. Accordingly, the most accurate *K*-structured sparse approximation of $\mathbf{x}$ that resides in the enlarged union of subspaces M_K^B is given by (Baraniuk 2007, Baraniuk 2010)

$$M_B(\mathbf{x}, K) = \arg\min_{\bar{\mathbf{x}} \in M_K^B} \left\| \mathbf{x} - \bar{\mathbf{x}} \right\|_2 . \tag{9}$$

2.3.2. Definition of the structure (Binary wavelet tree)

Inspired by theory of wavelet tree sparsity, the structure is defined as a tree model for wavelet coefficients. Supposing signal $\mathbf{x}$ of dimension $N = 2^I$, with *I* an integer value, the representation of $\mathbf{x}$ over a wavelet basis is of the form

$$\mathbf{x} = \vartheta_0 \boldsymbol{g} + \sum_{i=0}^{I-1} \sum_{j=0}^{2^i - 1} \omega_{i,j} \boldsymbol{\gamma}_{i,j} . \tag{10}$$

Where, $\boldsymbol{g}$ is the scaling function, $\boldsymbol{\gamma}_{i,j}$ denotes the wavelet function at scale *i* and offset *j*, υ_0 is the scaling coefficient, and $\omega_{i,j}$ represents wavelet coefficients at scale $0 \le i \le I-1$ and position $0 \le j \le 2^i - 1$. In light of $\mathbf{x} = \boldsymbol{\gamma}\mathbf{U}$, $\boldsymbol{\gamma}$ represents the scaling and wavelet functions as columns, and $\mathbf{U}$ represents the scaling and wavelet coefficients (Baraniuk 2007 and Baraniuk 2010). There is a parent/child relationship between the wavelet coefficients at different scales, where $\omega_{i+1,2j}$ and $\omega_{i+1,2j+1}$ are the children of $\omega_{i,j}$.

A set of wavelet coefficients Ω makes a connected sub-tree, if $\omega_{i,j} \in \Omega$ guarantees that its parent $\omega_{i-1,[j/2]} \in \Omega$. In this way, the set Ω will be a subspace of signals whose support resides in Ω, with all wavelet coefficients outside Ω zero. Accordingly, the structured sparsity model Γ_K is defined as the union of all possible *K*-dimensional subspaces pertaining to supports Ω that form connected subtrees.

The set of all *K*-tree sparse signals is defined as (Baraniuk 2007 and Baraniuk 2010)

$$\Gamma_K = \left\{ \mathbf{x} = \vartheta_0 \upsilon + \sum_{i=0}^{I-1} \sum_{j=1}^{2^i} \omega_{i,j} \psi_{i,j} : \omega\big|_{\Omega^C} = 0 \text{ s.t. } |\Omega| = K \text{ and } \Omega \text{ forms a subtree} \right\}. \tag{11}$$

Based on the above concept, the objective is now to seek $\Gamma(\mathbf{x}, K)$, i.e., the most accurate *K*-tree sparse solution over Γ_K, i.e.,

$$\Gamma(\mathbf{x}, K) = \arg\min_{\bar{\mathbf{x}} \in \Gamma_K} \left\| \mathbf{x} - \bar{\mathbf{x}} \right\|_2 . \tag{12}$$

To solve Eq. (12), *condensing sort and select algorithm* (CSSA) was implemented. In case the wavelet coefficients are monotonically increasing from the leaf to the root, $\Gamma(\mathbf{x}, K)$ is computed by easily sorting the wavelet coefficients. Otherwise, the CSSA solves the problem by condensing the nonmonotonic segments of the tree branches via an iterative sort-and-average scheme during a greedy search through the nodes. For further details, see Baraniuk and Jones (1994), Baraniuk (1999) and Baraniuk (2002). The tree-based CS scheme is outlined as follows.

Algorithm 1. The tree-based CS (Baraniuk 2007, Baraniuk 2010)

Initialize $i = 0$, $\mathbf{d} = \mathbf{y}$; $\mathbf{x}_0 = 0$	
While $\|\mathbf{e}\|_2 \geq \varepsilon$ **Do**	
$i \leftarrow i + 1$	
$\mathbf{e} = \mathbf{\tilde{u}}^T \mathbf{d}$	Update signal residual
assign $\text{supp}(\Gamma_2(\mathbf{e}, K))$ to q	Prune residual based on the structure
assign $\text{q} \cup \text{Supp}(\check{\mathbf{x}}_{i-1})$ *to* T	Add supports
$\mathbf{b}\big\|_T \leftarrow \mathbf{\tilde{u}}_T^+ \mathbf{y}, \quad \mathbf{b}\big\|_{T^C}$	Estimate signal, (+) denotes Moore-Pseudo inverse
$\check{\mathbf{x}}_i = \Gamma(\mathbf{b}, K)$	Prune signal estimate based on the structure
$\mathbf{d} = \mathbf{y} - \mathbf{\tilde{u}}\, \check{\mathbf{x}}_i$	Update the measurement residual
End Do	
$\check{\mathbf{x}} \leftarrow \check{\mathbf{x}}_i$	

2.4. Application of the CS to 3D EIT

In the sequel, the fast rough solution to the PCG is modeled as the compressive noisy measurement $\mathbf{y}$. It is done through assuming a fixed level of sparsity for the conductivity changes, so the blurred solution calculated by the PCG is considered as a noisy random transformation of the sparse conductivity field. The objective is thus to infer the *K*-tree sparse conductivity $\mathbf{x}$ from the blurred erroneous conductivity $\mathbf{y}$.

Theoretically, to exactly recover *K*-sparse $\mathbf{x}$ from $\mathbf{y} = \mathbf{\tilde{u}}\mathbf{x}$, $\mathbf{\tilde{u}} \in R^{M \times N}$ must satisfy the *K*-RIP condition. Many subgaussian random matrices satisfy the RIP with a high probability, e.g., Gaussian and Bernoulli (Rauhut 2010). From an application oriented perspective, pure random measurement matrices are typically of limited use in reality since they are not justifiable according to the application. Another drawback is that no

fast multiplication is available when such random matrices are applied (Rauhut 2010), so large-scale problems like 3D EIT will not be practicable using them.

To address such issues, structured random measurement matrix is formed as $\phi_{\kappa,j} = \omega_j(t_\kappa)$, where the structure is defined by functions ω_j, while the randomness is introduced by sampling locations t_κ.

In most application of the CS, the high degree of freedom of matrix $\mathbf{\acute{u}}$ aligning both κ and j disallows satisfying the RIP. To define a measurement matrix that can be bound according to the RIP, the problem is simplified such that it is merely focused on selecting support of $\mathbf{x}$, i.e., finite elements that contain the salient information over the conductivity field, rather than the exact calculation of $\mathbf{x}$ itself. To reach this purpose, structured random partial Fourier matrix is applied. To define the structure for each independent measurement $\kappa = 1,...,M$, the discrete Fourier transform is computed over $j = 1,...,N$ as follows (Rauhut 2010).

$$y(\kappa) = \sum_{j=1}^{N} x_j \phi_{\kappa,j} = \sum_{j=1}^{N} x_j \omega_j(t_\kappa) = \sum_{j=1}^{N} x_j e^{i2\pi\kappa j/N} \tag{13}$$

The randomness is introduced by random parameters $t_k, \kappa = 1,...,M$, i.e., randomly sorting the rows of $\mathbf{\acute{u}}$. By fixing $\mathbf{\acute{u}}$ over each column $j = 1,...,N$ and allowing the freedom solely over rows $\kappa = 1,...,M$, the sparse solution $\check{\mathbf{x}}$ is calculated in a way in which the exact solution of $\check{\mathbf{x}}$ is lost in exchange for the exact selection of indices including the desired *K*-sparsity. From the 3D EIT oriented perspective, the exact conductivity change over the finite elements is lost at the cost of exactly selection of the *K* finite elements pertaining to support of $\check{\mathbf{x}}$.

2.5. Application of sparse recovery inverse solvers

The choice of $r = 1$ conducts Eq. (2) to the sparse recovery. The ill-posedness of the ℓ_1 recovery specifically depends on the ratio of the number of the unknown parameters to the data size. It will be shown that applying the sparse recovery solvers solely to the finite elements selected by the CS, rather than to the whole domain, appreciably improves the accuracy of the solution. In this way, the conductivity change over the unselected finite elements is set to background, so the degree of freedom of the problem is significantly reduced. Furthermore, sparse recovery codes considerably benefit from a good initialization. This suggests that the solution to the CS ($\check{\mathbf{x}}$) is considered as the initial point.

Theoretical and numerical studies have demonstrated the superiority of the GPSR and SpaRSA with regard to both accuracy and speed over a wide range of sparse recovery solvers (Figueiredo *et al* 2007, Wright *et al* 2009). In addition, to best of our knowledge, TVAL3 outperforms other total variation solvers (Li 2009). Accordingly, this study applies the proposed CS-based scheme to the SpaRSA, GPSR and TVAL3. These solvers are, respectively, detailed in Appendices A, B and C.

3. Numerical results

3.1. Simulated model A

A cylindrical phantom was simulated with a normalized dimension, i.e., 1 in radius and 3 in height. The mesh was made up of 57024 finite elements. Thirty two electrodes were simulated based on the complete electrode model with a contact impedance of $100\,\Omega$ per electrode, and attached to the surface of the phantom in accordance with the planar electrode placement configuration (Graham and Adler 2007). The background conductivity was set to $1\,\mathrm{Sm}^{-1}$. Two inclusions having conductivities of $0.5\,Sm^{-1}$ and $1.5\,Sm^{-1}$ were placed at $z=[-0.5909,-0.4091]$ and $z=[+0.3182,+0.5000]$, respectively. Figure 1 exhibits the phantom and the contained inclusions. The simulated data was contaminated with a 20 db additive white Gaussian noise (AWGN).

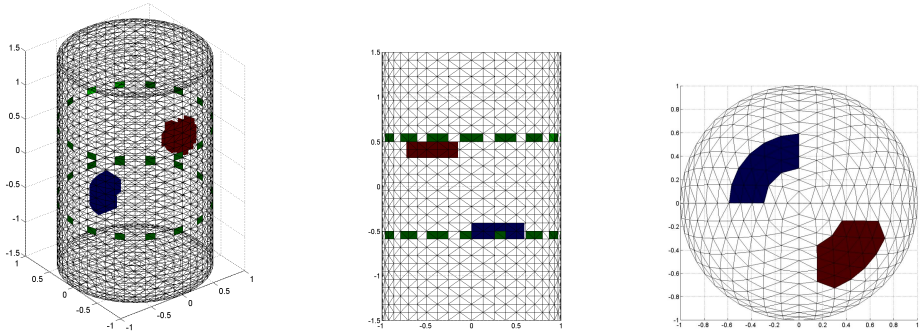

(a) (b) (c)

Figure 1. Simulated model A from: (a) a 3D view, (b) a lateral view, and (c) a top view.

3.1.1. Fast application of the PCG with a great stopping threshold (Stage 1)

To solve the inverse problem, a homogenous mesh constituted of 12288 tetrahedral elements was created. The PCG solver was implemented with two different terminating thresholds. Figure 2(a) and (b), respectively, display the solution to PCG terminated at $\varepsilon_1 = 8e-1$ and $\varepsilon_2 = 1e-2$. $\varepsilon_1 = 8e-1$ was applied to make a fast rough

estimate of the conductivity changes, as discussed in section 2, while ε_2 yields the optimized solution among all the iterations. The criterion for the optimization is relative error (RE), i.e.,

$$\mathrm{RE} = \frac{\left\| \breve{\mathbf{u}}\mathring{\mathbf{u}}_{\text{solution}} - \breve{\mathbf{u}}\mathring{\mathbf{u}}_{\text{simulated}} \right\|_2}{\left\| \breve{\mathbf{u}}\mathring{\mathbf{u}}_{\text{simulated}} \right\|_2} \times 100, \tag{14}$$

where $\breve{\mathbf{u}}\mathring{\mathbf{u}}_{\text{simulated}}$ is calculated by mapping the simulated conductivity changes over the forward mesh onto the inverse mesh. The solution at ε_2 was used as a benchmark to compare the standard PCG to the proposed CS-based approach.

3.1.2. Application of the CS for selecting the finite elements representing K-sparsity (Stage 2)

The sparsity level of the solution to the CS ($\breve{\mathbf{x}}$) was set to 1000. Therefore, almost 0.08 of the voxels were selected for the sparse recovery, and the conductivity change over the remaining voxels was set to zero. In this way, the condition number of the Jacobian ($\mathbf{J}$) was reduced from 2.02×10^{19} to 1.07×10^{16}. In figure 2(d), the blue areas represent the selected finite elements over the different slices.

3.1.3. Application of the sparse inverse solvers to the selected voxels (Stage 3)

In light of Appendix A, the SpaRSA algorithm was implemented by $\lambda = 1e-6$, $\alpha_{\min} = 1e-30$, $\alpha_{\max} = 1e+30$, $\eta = 2$, $\mu = 0.01$, $Q = 5$ and $tolp = 0.01$. The parameters were heuristically chosen so that the solution produces the minimal RE. The dependency of the RE on λ was much more than the other parameters. The SpaRSA was first applied to the whole domain in a standard manner with an initial guess of zero, and produced the image shown in figure 2(c). It was then applied solely to the selected 1000 finite elements with the solution to the CS as its initial guess. Figure 2(e) shows the image reconstructed by the proposed CS-based scheme. The slices were chosen evenly at heights written to the left of the figure. The colorbars are indicated to the right of each image.

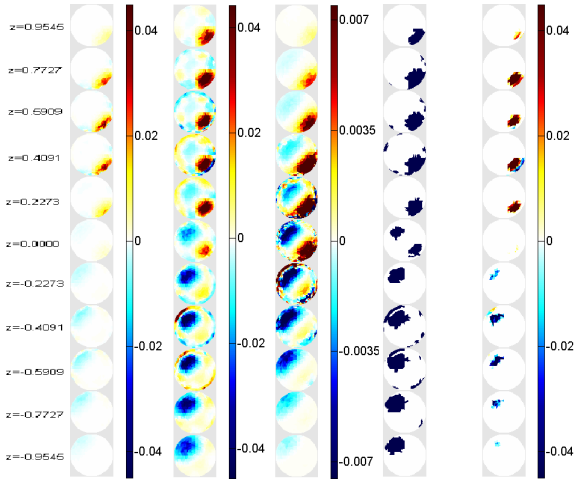

(a) (b) (c) (d) (e)

Figure 2. The images of model A, calculated by: (a) the PCG at $\varepsilon_1 = 8e-1$, (b) the PCG at $\varepsilon_2 = 1e-2$, and (c) the standard SpaRSA. (d) The finite elements sampled by the CS, and (e) the image calculated by the CS-based SpaRSA.

Comparing figure 2(b), (c) and (e) to figure 1 demonstrates that the proposed CS-based scheme has produced more accurate image, compared to the customary application of the PCG or SpaRSA. As shown in figure 2(b), the standard PCG reconstructed an image with a low spatial resolution. Figure 2(c) indicates that the pure SpaRSA has produced a misleading image. Figure 2(e), however, demonstrates that the CS has considerably improved the spatial resolution aligning both axial and vertical planes.

To show the performance of the CS on the GPSR, it was implemented by $\lambda = 1e-5$, $\alpha_{\min} = 1e-30$, $\alpha_{\max} = 1e+30$ and $tolp = 0.01$, according to Appendix B. Figure 3(a) and (b) display the images reconstructed by the standard and CS-based GPSR, respectively.

In light of Appendix C, the TVAL3 was implemented by $\mu = 2^{11}$, $\beta_i = 2^8$ for all i, inner $\text{tol} = 1e-4$, outer $\text{tol} = 1e-5$, and $\delta = 1e-5$. The standard TVAL3 was initialized by zero, so η was set to be close to 1, i.e., $\eta = 0.995$. Figure 3(c) exhibits the image reconstructed by the standard TVAL3. The CS-based TVAL3 was initialized by the solution to the CS, so η was set to be close to zero, i.e., $\eta = 0.3$, as the choice of η greatly depends on closeness of the initialization to the optimum. Figure 3(d) shows the image reconstructed by the CS-based TVAL3. As shown in figure 3 (a) and (c), applying both the GPSR and TVAL3 in a standard way has led to

misleading results. The CS scheme, however, improved the solution appreciably, as observable in figure 3(b) and (d).

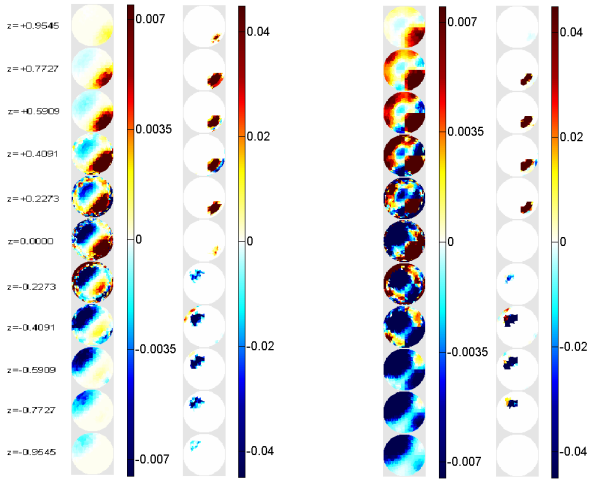

(a) (b) (c) (d)

Figure 3. The images of model A, reconstructed by: (a) the standard GPSR, (b) the CS-based GPSR, (c) the standard TVAL3, and (d) the CS-based TVAL3.

3.2. Simulated model B

The forward and inverse meshes were created in the same way as applied to model A. Three inclusion having conductivities of $2\,Sm^{-1}$, $1.5\,Sm^{-1}$ and $0.5\,Sm^{-1}$ were placed at $z=[-0.8636,-0.6818]$, $z=[+0.7727,+0.9545]$ and $z=[+0.0455,+0.2273]$, respectively. Figure 4 shows the simulated tank. The simulated data was polluted with a 20 db AWGN noise.

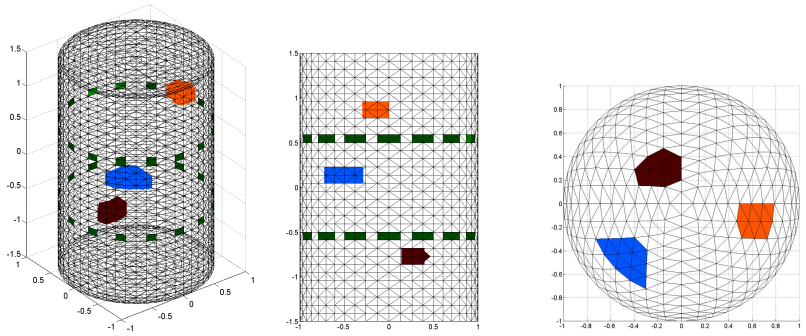

(a) (b) (c)

Figure 4. Simulated model B from: (a) a 3D view, (b) a lateral view, and (c) a top view.

The PCG solver was first employed, and the images were reconstructed at $\varepsilon_1 = 5e-1$ and $\varepsilon_2 = 1e-2$, as shown in figure 5(a) and (b), respectively. Figure 5 (d)

exhibits the 1000 finite elements selected by the CS algorithm. Figure 5 (c) and (e), respectively, show the images calculated by the standard and the CS-based SpaRSA.

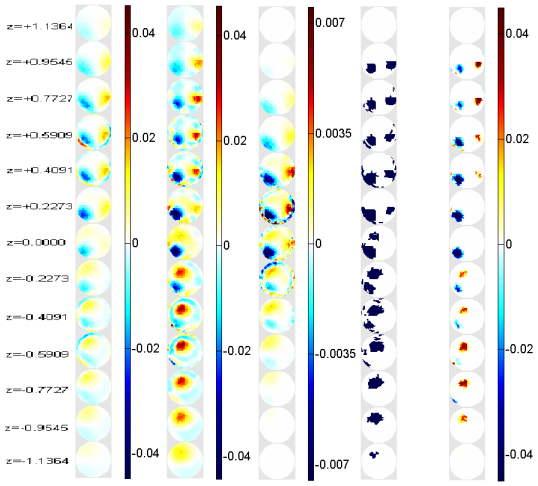

(a) (b) (c) (d) (e)

Figure 5. The images of model B, calculated by: (a) the PCG at $\varepsilon_1 = 5e-1$, (b) the PCG at $\varepsilon_2 = 1e-2$, and (c) the standard SpaRSA. (d) The finite elements sampled by the CS, and (e) the image calculated by the CS-based SpaRSA.

As observable in figure 5(b), the standard PCG produced an image with a low spatial resolution and a large amount of artefact. Figure 5(c) demonstrates that the standard SpaRSA reconstructed a misleading image. However, as shown in figure 5(e), the CS-based SpaRSA remarkably improved the solution.

In a similar way, figure 6(a) and (b), respectively, show the images reconstructed by the standard and the CS-based GPSR. The images reconstructed by the standard and the CS-based TVAL3 are also displayed in figure 6(c) and (d), respectively. As shown in figure 6, the CS-based solvers produced much more accurate image regarding the spatial resolution and the artefact, compared to the competing pure solvers.

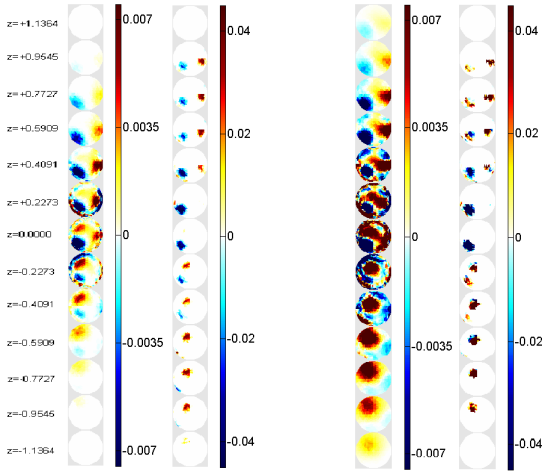

(a) (b) (c) (d)

Figure 6. The images of model B, reconstructed by: (a) the standard GPSR, (b) the CS-based GPSR, (c) the standard TVAL3, and (d) the CS-based TVAL3.

3.3. Simulated model C (breast tumours)

A breast phantom was simulated with a normalized dimension, i.e., 1.5 in height and 1 in radius of the top plane. The phantom was made up of 150218 tetrahedral elements. Sixteen electrodes with a contact impedance of $100\,\Omega$ were divided into two planes, and were evenly attached to the surface of the phantom. The background conductivity was set to $1\,\mathrm{Sm}^{-1}$. Two spherical tumours were simulated, one of which with a conductivity of $2\,\mathrm{Sm}^{-1}$ and a radius of 0.12, and another with a conductivity of $3\,\mathrm{Sm}^{-1}$ and a radius of 0.10. The data were contaminated with a 20 db AWGN noise. Figure 7 displays the breast model.

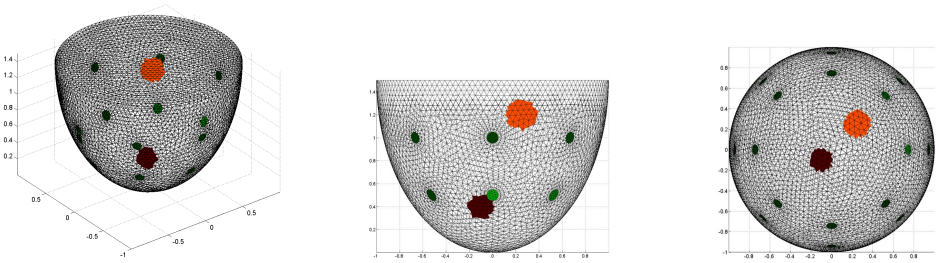

(a) (b) (c)

Figure 7. Simulated breast model C from: (a) a 3D view, (b) a lateral view, and (c) a top view.

To solve the inverse problem, a coarse mesh made up of 13101 voxels was used. Figure 8(a) and (b), respectively, show the images calculated by the PCG at $\varepsilon_1 = 9e-1$ and $\varepsilon_2 = 3e-2$. ε_2 denotes the stopping threshold that minimizes the RE. The CS was then applied to reduce the number of the voxels to 1000. The conductivity change over the remaining voxels was set to zero. As a result, the condition number of the Jacobian was reduced from 1.85×10^{18} to 5.34×10^{15}. In Figure 8(d), the finite elements selected by the CS were represented by the blue areas. Finally the SpaRSA solver was applied to the model. Figure 8(c) displays the image reconstructed by the standard SpaRSA initialized at zero, and figure 8(e) shows the image reconstructed by the CS-based SpaRSA.

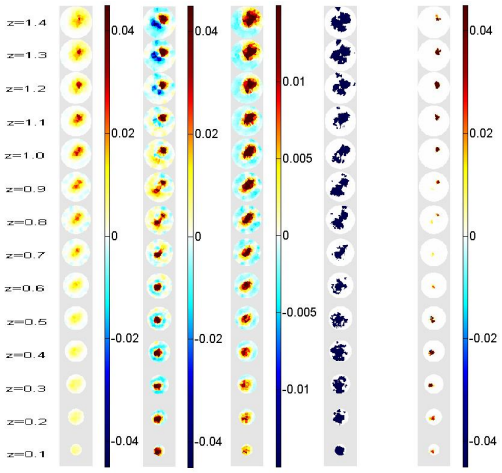

(a) (b) (c) (d) (e)

Figure 8. The images of the breast model C, calculated by: (a) the PCG at $\varepsilon_1 = 9e-1$, (b) the PCG at $\varepsilon_2 = 3e-2$, and (c) the standard SpaRSA. (d) The finite elements sampled by the CS, and (e) the image calculated through the CS-based SpaRSA.

As observable in figure 8(b) and (c), the standard application of the PCG and SpaRSA has led to images with a low spatial resolution. These standard solvers produced a misleading representation of the tumours. However, as shown in figure 8(e), the proposed CS-based SpaRSA significantly improved the spatial resolution, and reduced the artefact. It better determined the size and location of the tumours, compared to the competing standard solvers.

Figure 9(a) and (b), respectively, display the images reconstructed by the standard and CS-based GPSR, while figure 9(c) and (d) pertain to the images calculated by the standard and CS-based TVAL3 solvers. This figure affirms the capability of the CS in improving performance of the sparse recovery in determining breast tumours.

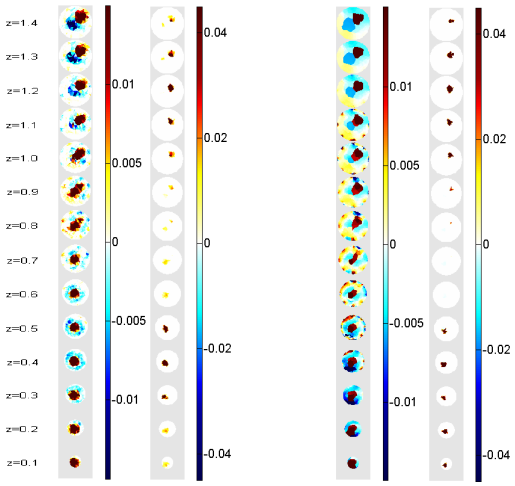

(a) (b) (c) (d)

Figure 9. The images of breast model C, reconstructed by: (a) the standard GPSR, (b) the CS-based GPSR, (c) the standard TVAL3, and (d) the CS-based TVAL3.

3.4. Computational cost and Figures of merit

Execution time elapsed at each stage of the proposed scheme was computed, and the total time was compared to that of the standard PCG and the employed pure sparse solvers. Note that the PCG solution calculated at the optimal threshold (ε_2) represents the standard PCG. Table 1 shows the CPU time elapsed by the competing inverse solvers. According to this table, although the proposed CS-based approach consists of three stages, the total CPU time was still smaller than that of the standard PCG. The CPU time was, however, slightly greater than that of the standard SpaRSA and GPSR. Note that the standard sparse codes have produced misleading results. The CS-based TVAL3, however, was faster than the standard TVAL3. Indeed, total variation inverse solvers are typically slower than sparse recovery codes, as the TV minimization deals with the Gradient of the conductivity, rather than the conductivity itself.

Table 1. The CPU time (Sec) elapsed by the inverse solvers.

Simulated Simulated phantom	Solvers	PCG PCG at ε_1		PCG PCG at ε_2		Standard Standard ℓ_1 solver		CS		ℓ_1 solver after CS		CS-based method (total)
A	SpaRSA GPSR TVAL3	0.81		1.31		0.80 0.96 1.73		0.23		0.11 0.15 0.32		1.15 1.19 1.36
B	SpaRSA GPSR TVAL3	0.85		1.37		0.91 1.12 1.89		0.19		0.13 0.11 0.43		1.17 1.15 1.47
C	SpaRSA GPSR TVAL3	1.02		1.64		1.14 1.26 2.31		0.25		0.18 0.22 0.35		1.45 1.49 1.62

Table 2 evaluates the performance of the solvers with respect to the RE. According to this table, the standard PCG performs more accurately than the standard ℓ_1 solvers in determining the inclusions. Considering each simulated phantom, the RE of the solution to the PCG was smaller than that of all the pure sparse recovery codes. The

CS scheme, however, improved the accuracy of the solution to the sparse codes remarkably, and produced images with an RE much smaller than that of the PCG. Furthermore, a comparison between the standard ℓ_1 solvers clarifies that the SpaRSA was slightly better than the GPSR regarding both the accuracy and time. The standard TVAL3 was the worst solver, as the TV minimization typically deals with piecewise conductivity fields to produce sharp edges (Borsic *et al* 2010), rather than small inclusions. The CS, however, considerably improved the performance of the TVAL3 regarding both accuracy and time, making it as efficient as the other proposed CS-based solvers in dealing with small inclusions. There were no significant differences between the CS-based SpaRSA and GPSR regarding both the RE and CPU time.

Table 2. The Relative Error (%) of the reconstructed images

Simulated phantom		PCG at ε_2 (standard)		Standard ℓ_1 solver		CS-based ℓ_1 solver
A	SpaRSA GPSR TVAL3	95.75		99.04 100.78 125.45		78.67 79.33 76.92
B	SpaRSA GPSR TVAL3	97.76		109.34 111.23 120.56		69.73 69.17 70.15
C	SpaRSA GPSR TVAL3	102.87		111.44 113.91 115.76		66.27 64.68 65.41

4. Experimental results

To validate the performance of the proposed scheme in real cases, the solvers were applied to an experimental 3D data available on the EIDORS website (http://eidors3d.sourceforge.net). A cylindrical phantom, 30 cm in diameter and height, was filled with 0.9% saline solution. Sixteen electrodes were divided into two rings. The data was collected according to the zigzag-offset protocol (Graham and Adler 2007). Two nonconductive golf balls having a radius of 2cm were located in the following positions. The inverse solvers were applied to an inhomogeneous mesh made up of 50645 finite elements.

4.1. Object 1 at (7,0,10) cm and object 2 at (0,7,10) cm

Figure 10 (a) shows the image reconstructed by the standard PCG terminated at the optimal point ($\varepsilon_2 = 2e-2$). Figure 10 (b) and (d), respectively, display the optimal images reconstructed by the standard SpaRSA and GPSR. Figure 10 (c) and (e) exhibit the images reconstructed by the CS-based SpaRSA and GPSR through sampling 2000 finite elements from the solution to PCG calculated at $\varepsilon_2 = 9e-1$.

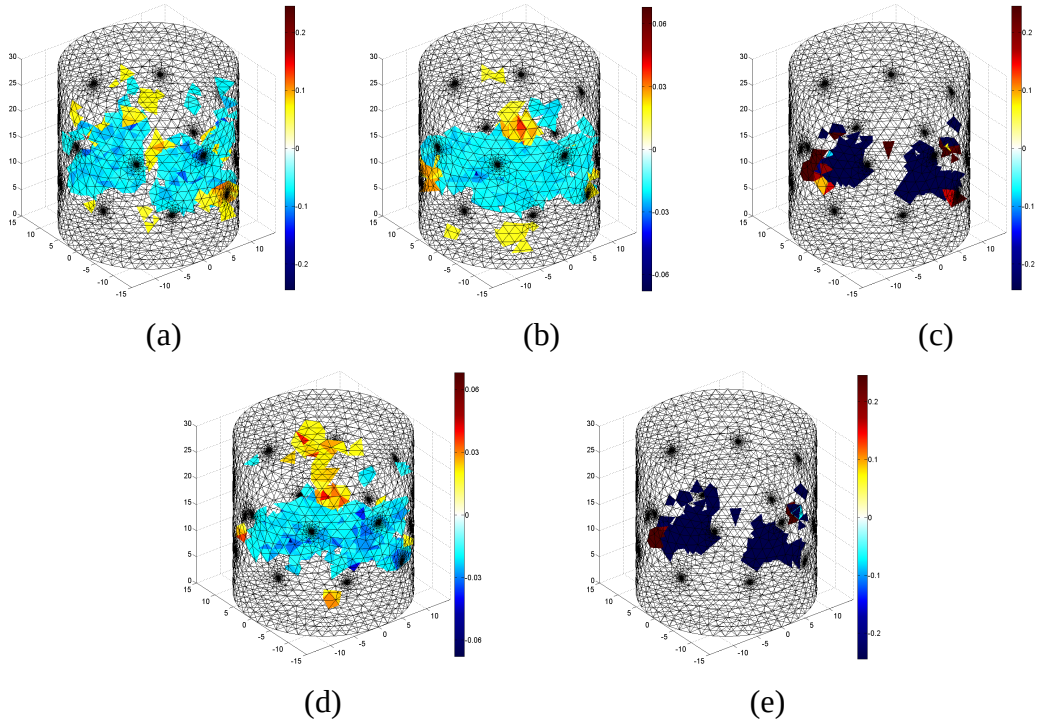

(a) (b) (c)

(d) (e)

Figure 10. The 3D images of the first experimental data, reconstructed by: (a) the PCG at $\varepsilon_2 = 2e-2$, (b) the standard SpaRSA, (c) the CS-based SpaRSA, (d) the standard GPSR, and (e) the CS-based GPSR.

As a result of the inhomogeneity of mesh density, which is much finer near the electrodes than the central regions, the RE resigns to deal with the differences between size of the finite elements. The solvers were thus optimized in terms of the RES volume instead, i.e., the volume of the inverse mesh involving finite elements with an absolute conductivity change greater than 0.25 of the maximal absolute conductivity change.

4.2. Object 1 at (7,0,10) cm and object 2 at (0,7,20) cm

Figure 11 shows the reconstructed images in the same way as applied to the first data.

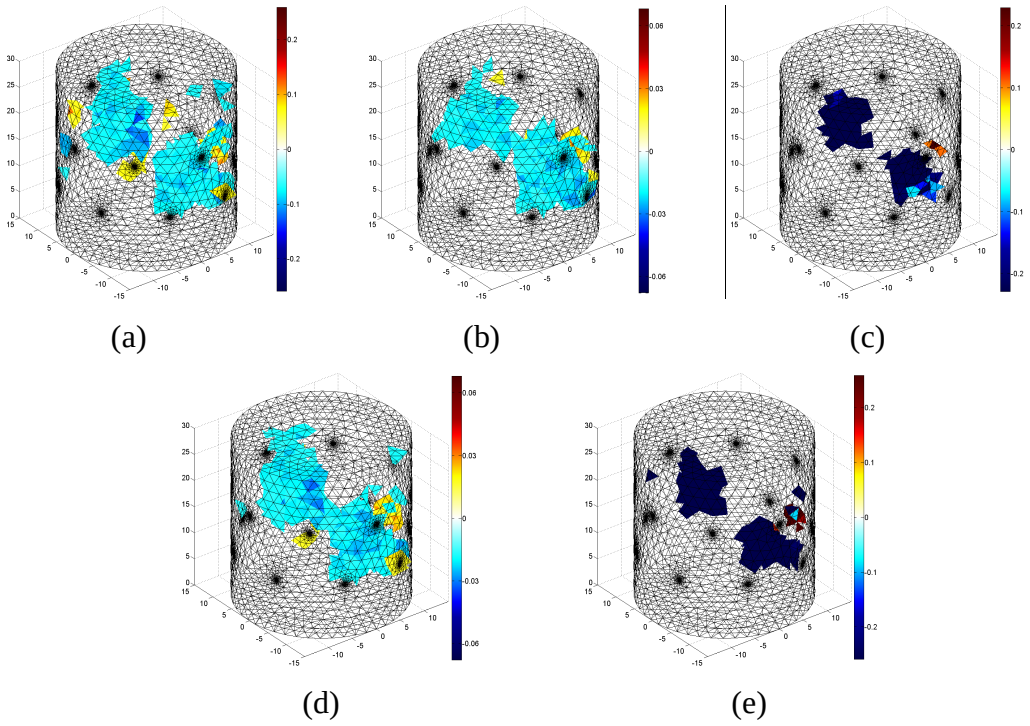

(a) (b) (c)

(d) (e)

Figure 11. The 3D images of the second experimental data, reconstructed by: (a) the PCG at $\varepsilon_2 = 2e-2$, (b) the standard SpaRSA, (c) the CS-based SpaRSA, (d) the standard GPSR, and (e) the CS-based GPSR.

Table 3 compares the ratio of the RES volume for each image to the true volume of the golf balls. According to this table, the CS has improved the RES approximately three times, compared to the standard solvers.

Table 3. The ratio of the RES volume to the true volume of the golf balls for each reconstructed image

Experimental data		PCG at ε_2 (standard)		Standard ℓ_1 solver		CS-based ℓ_1 solver
1	SpaRSA GPSR	17.87		19.34 20.16		6.63 5.86
2	SpaRSA GPSR	15.74		16.43 17.08		6.13 6.77

5. Discussion

This study proposed a CS-based approach to deal with large-size 3D EIT, as the existence of a large number of finite elements causes significant problems regarding convergence and speed. Indeed, the large number of degrees of freedom of the

problem in such cases gives rise to a severely ill-posed inverse problem. Adoption of a coarse inverse mesh is an alternative to moderating the ill-posedness, but deteriorates the spatial resolution considerably, especially when the conductivity field involves small-sized inclusions.

Sparse recovery has aroused growing interest in EIT, but the large size of the forward operator in 3D cases affects its performance deleteriously. The proposed method mitigates the high ill-posedness of the sparse solvers via conducting the solution solely to the voxels containing the salient information of the conductivity field, at the same time setting the conductivity over the unselected voxels to background. This method was initialized by a PCG solver, which produces a fast blurred estimate of the conductivity at the first stage. A CS-based algorithm was then applied to sample voxels based on assuming a fixed level of sparsity on the solution. In this way, a sparse representation of the domain that contains the true solution was estimated from the rough solution to the PCG. The ℓ_1 recovery codes were finally applied merely to the selected finite elements, with the solution to CS as the initial guess. The results showed that the proposed scheme significantly improved the accuracy of solution to ℓ_1 recovery codes. Further studies need to be done to find a way to applying the compressed sampling theory directly to the forward operator so that the finite elements are sampled without the need for the preprocessing PCG solver. Indeed, the sever ill-posedness of the forward operator in 3D EIT is the main impediment to this aim.

6. Conclusion

There are many cases in medical applications of 3D EIT, where the organ under study involves small inclusions. Such cases arise for example in determination of tumours in breast. The results show the great capability of the proposed CS-based scheme in studying organs that represent an approximately homogenous conductivity field plus some small-sized inclusions. The authors anticipate that the proposed algorithm can open a new way to 3D application of EIT for imaging breast tumours. The proposed algorithm was applied to time-difference EIT. Further studies are needed to apply it to frequency-difference EIT, which is the case in imaging of breast tumours (Seo *et al* 2008).

Appendix A. Sparse Reconstruction by Separable Approximation (SpaRSA)

The framework is based on Wright *et al* (2009), and is available on (http://www.lx.it.pt/~mtf/SpaRSA).

Consider the unconstrained optimization problem of the form

$$\min_x \ \phi(x) = f(x) + \lambda c(x) \tag{A.1}$$

The rationale behind this approach is to generate a sequence of iterates $\{x^k, k = 0,1,...\}$, which conducts Eq. (A.1) to a class of problems where the following subproblem can be solved efficiently under some conditions on *f* and *c*.

$$x^{k+1} \in \arg\min_z \ (z - x^k)^T \nabla f(x^k) + \frac{\alpha_k}{2}\left\|z - x^k\right\|_2^2 + \lambda c(z) \tag{A.2}$$

for $\alpha_k \in R^+$. Problem (A.2) can be casted in the form

$$x^{k+1} \in \arg\min_z \ \frac{1}{2}\left\|z - u^k\right\|_2^2 + \frac{\lambda}{\alpha_k} c(z), \tag{A.3}$$

where

$$u^k = x^k - \frac{1}{\alpha_k}\nabla f(x^k). \tag{A.4}$$

The function $c(x) = \sum_{i=1}^{n} c_i(x_i)$, which is separable into the sum of functions of its individual components, satisfies the conditions on (A.2) to a high degree. Accordingly, Eq. (A.3) can be separated in the form

$$x_i^{k+1} \in \arg\min_z \frac{(z - u_i^k)^2}{2} + \frac{\lambda}{\alpha_k} c_i(z), \ \ i = 1,2,...,N. \tag{A.5}$$

Considering $c(z) = \|z\|_1$, which yields $c_i(z) = |z|$ for all *i*, Eq. (A.5) will be of the form

$$x_i^{k+1} \in \arg\min_z \frac{(z - u_i^k)^2}{2} + \frac{\lambda|z|}{\alpha^k} = \text{soft}\left(u_i^k, \frac{\lambda}{\alpha^k}\right), \tag{A.6}$$

where $\text{soft}(u, a) \equiv \text{sign}(u)\max\{|u| - a, 0\}$.

Algorithm 2. SpaRSA

Set $\eta > 1$ and $[\alpha_{\min}, \alpha_{\max}] \in (0, \infty)$

Initialize x^0; $k = 0$

While stopping criterion is not satisfied **Do**

Choose $\alpha^k \in [\alpha_{\min}, \alpha_{\max}]$

While acceptance criterion is not satisfied by x^{k+1} **Do**

Calculate x^{k+1} through Eq. (A.6)

Set $\alpha^k \leftarrow \eta\,\alpha^k$

End Do

Set $k \leftarrow k+1$

End Do

Employing the Barzilai-Borwein (BB) scheme, we choose α^k such that $\alpha^k I$ approaches the Hessian $\nabla^2 f(x)$ over the latest step. Letting $s^k = x^k - x^{k-1}$ and $r^k = \nabla f(x^k) - \nabla f(x^{k-1})$, it yields

$$\alpha^k = \arg\min_{\alpha} \left\| \alpha s^k - r^k \right\|_2^2 = \frac{(r^k)^T r^k}{(r^k)^T s^k}. \tag{A.7}$$

The inner loop in SpaRSA is to solve subproblem (A.6) by a sequence of α^k and then to accept x^{k+1} when an acceptance criterion is satisfied. The BB approach is usually implemented in a nonmonotonic fashion, so x^{k+1} is accepted as a new iterate, even if it increases the objective function. The acceptance criterion is the globally convergent Barzilai-Borwein criterion, where x^{k+1} is accepted as a new iterate if the objective function is smaller than the largest objective function over the previous $Q+1$ iterations. In this way, x^{k+1} is accepted if

$$\varphi(x^{k+1}) \le \max_{i=\max(k-Q,0),\ldots,k} \varphi(x^k) - \frac{\mu}{2}\alpha^k \left\| x^{k+1} - x^k \right\|^2, \tag{A.8}$$

where Q is a fixed integer, and $\mu \in (0,1)$ is a constant that is often chosen near zero.

Appendix B. Gradient Projection for Sparse Reconstruction (GPSR)

The framework is based on Figueiredo *et al* (2007), and is available on (http://www.lx.it.pt/~mtf/GPSR).

Consider the convex unconstrained optimization problem

$$\min_x \frac{1}{2}\|y - Ax\|_2^2 + \lambda \|x\|_1. \tag{B.1}$$

The base of this approach is to split x into its positive and negative parts, i.e.,

$$x = u - v, \quad u \ge 0, v \ge 0, \tag{B.2}$$

where $u_i = (x_i)_+$ and $v_i = (-x_i)_+$ for all $i = 1,2,\ldots,N$, with $(x)_+ = \max\{0, x\}$. The problem (B.1) can now be rewritten as

$$\min_{u,v} \frac{1}{2}\left\|y - A(u-v)\right\|_2^2 + \lambda 1_n^T u + \lambda 1_n^T v \quad \text{s.t.} \quad u \geq 0, v \geq 0 . \tag{B.3}$$

Considering $z = \begin{bmatrix} u \\ v \end{bmatrix}$, $c = \lambda 1_{2n} + \begin{bmatrix} -A^T y \\ A^T y \end{bmatrix}$ and $B = \begin{bmatrix} A^T A & -A^T A \\ -A^T A & A^T A \end{bmatrix}$, the problem (B.3) can be casted in the form

$$\min_z c^T z + \frac{1}{2} z^T B z \equiv F(z) \quad \text{s.t.} \quad z \geq 0 . \tag{B.4}$$

Applying Gradient Projection technique to problem (B.4) yields

$$w^k = (z^k - \alpha^k \nabla F(z^k))_+ . \tag{B.5}$$

A backtracking line search is then performed over $\tau^k \in [0,1]$ in the form

$$z^{k+1} = z^k + \tau^k (w^k - z^k) . \tag{B.6}$$

Considering

$$g_i^k = \begin{cases} \nabla F(z^k)_i, & \text{if} \quad z_i^k > 0 \; or \; (\nabla F(z^k))_i < 0 \\ 0, & \text{otherwise} \end{cases}, \tag{B.7}$$

α^0 is selected to be the exact minimizer of F along g^k, i.e.,

$$\alpha^0 = \arg\min_{\alpha} F(z^k - \alpha g^k) . \tag{B.8}$$

An upper and lower bounds are often considered for α^0, i.e., $\alpha^0 \in [\alpha_{\min}, \alpha_{\max}]$. By applying the BB scheme, the GPSR algorithm is outlined as follows.

Algorithm 3. GPSR

Set $k = 0$

Choose $\alpha^0 \in [\alpha_{\min}, \alpha_{\max}]$

While stopping criterion is not satisfied **Do**

Calculate $\delta^k = (z^k - \alpha^k \nabla F(z^k))_+ - z^k$

Backtracking line search: Calculate $\tau^k \in [0,1]$ that minimizes $F(z^k + \tau^k \delta^k)$

Set $z^{k+1} = z^k + \tau^k \delta^k$

$\gamma^k = (\delta^k)^T B \delta^k$

If $\gamma^k = 0$

$\alpha^{k+1} = \alpha_{\max}$, otherwise

$$\alpha^{k+1} = \text{mid}\left\{\alpha_{\min}, \frac{\left\|\delta^k\right\|_2^2}{\gamma^k}, \alpha_{\max}\right\}$$

$k \leftarrow k+1$

End Do

The stopping criterion for both the SpaRSA and GPSR was motivated by perturbation results for linear complementarity problems, which is defined as

$$\left\|\min(z, \nabla F(z)\right\| \le tolp\,. \tag{B.9}$$

Appendix C. Total Variation minimization through augmented Lagrangian and alternating direction method (TVAL3)

The framework is based on Li (2009), and is available on (http://www.caam.rice.edu/~optimization/L1/TVAL3).

The constrained variant of total variation minimization is of the form

$$\min_x \sum_i \left\|D_i x\right\|_1 \quad \text{s.t.} \quad y = Ax\,, \tag{C.1}$$

where $D_i x$ denotes discrete gradient of x at index i. In 3D EIT, $D_i x$ represents the jump of the conductivity change over every two neighboring finite elements. Problem (C.1) can be casted in the form

$$\min \sum_{w_i, x} \left\|w_i\right\| \qquad \text{s.t.} \quad y = Ax,\ w_i = D_i x \text{ for all } i\,. \tag{C.2}$$

The so-called alternating direction method yields

$$\begin{aligned}\min_{w_i, x} L_A(w_i, x) = \sum_i \Big(\left\|w_i\right\| - \nu_i^T (D_i x - w_i) + \frac{\beta_i}{2}\left\|D_i x - w_i\right\|_2^2\Big) \\ - \rho^T (Ax - y) + \frac{\mu}{2}\left\|Ax - y\right\|_2^2\end{aligned} \tag{C.3}$$

The augmented Lagrangian function is first minimized with respect to w_i, i.e.,

$$w_i^{k+1} = \max\left\{\left|D_i x^k - \frac{\nu_i}{\beta_i}\right| - \frac{1}{\beta_i}, 0\right\} \operatorname{sgn}\left(D_i x^k - \frac{\nu_i}{\beta_i}\right)\,. \tag{C.4}$$

The AL function at w_i^{k+1} is then minimized with respect to x as follows.

$$\begin{aligned}\min_x L_A(w_i^{k+1}, x) = \min_x [Q^k(x) = \sum_i \Big(-\nu_i^T (D_i x - w_i^{k+1}) + \frac{\beta_i}{2}\left\|D_i x - w_i^{k+1}\right\|_2^2\Big) \\ - \rho^T (Ax - y) + \frac{\mu}{2}\left\|Ax - y\right\|_2^2]\end{aligned} \tag{C.5}$$

The gradient of $Q^k(x)$ is calculated in the form

$$d^k(x) = \sum_i (\beta_i D_i^T(-D_i x - w_i^{k+1}) - D_i^T \nu_i) + \mu A^T(Ax - y) - A^T \rho. \quad \text{(C.6)}$$

The costly calculation of pseudoinverse in large-scale problems encourages steepest descent method to solve Eq. (C.5), i.e., recurrence formula $\tilde{x} = x - \alpha d$.

The steepest descent requires iteratively calculating $d^k(x)$, which is still too costly for large-scale problems like 3D EIT. However, it turns out that only one step can still guarantee the convergence of the algorithm, which yields

$$x^{k+1} = x^k - \alpha^k d^k. \quad \text{(C.7)}$$

To choose α^k, the BB scheme was used, i.e.,

$$\alpha^k = \frac{(s^k)^T s^k}{(s^k)^T r^k}, \quad \text{(C.8)}$$

where $s^k = x^k - x^{k+1}$ and $r^k = d^k(x^k) - d^k(x^{k-1})$. To accept the BB step, a nonmonotone line search was applied, which checks the nonmotone Armijo condition, i.e.,

$$Q^k(x^k - \alpha^k d^k) \le C^k - \delta \alpha^k (d^k)^T d^k. \quad \text{(C.9)}$$

Where, C^k is updated in the form

$$P^{k+1} = \eta P^k + 1$$

$$C^{k+1} = (\eta P^k C^k + Q^k(x^{k+1}))/P^{k+1}. \quad \text{(C.10)}$$

Where, δ and η are set between 0 and 1. The best convergence is obtained by η close to 1 for the initial point far from the optimum and close to zero when near the optimum. In the sequel, the TVAL3 is outlined.

Algorithm 4. Alternating Direction Method

Set $0 < \delta, \eta, \vartheta < 1$ and w_i^0, x^0

$C^0 = L_A(w_i^0, x^0)$

While $\frac{\left\|x^{k+1} - x^k\right\|_2}{\left\|x^k\right\|_2} \ge$ inner tol **Do**

Calculate w_i^{k+1} through (C.4)

Calculate d^k through (C.6)

Set α_k through (C.8)

While (C.9) is unsatisfied **Do** (Nonmonotone Armijo loop)

Set $\alpha^k = \vartheta\alpha^k$ (backtracking)

End Do

Calculate x^{k+1} through (C.7)

Set C^{k+1} through (C.10)

End Do

Algorithm 5. TVAL3

Set $\nu_i^0, \beta_i^0, \rho^0, \mu^0$ and w_i^0, x^0 for all *i*

While $\dfrac{\left\|x^{t+1} - x^t\right\|_2}{\left\|x^t\right\|_2} \geq$ outer tol **Do**

Set $w_i^{0(t+1)} = w_i^t$, $x^{0(t+1)} = x^t$

Calculate minimizers of problem (C.3), w_i^{t+1} and x^{t+1} , through Algorithm (4)

Update ν_i^t, ρ^t according to w_i^{t+1} and x^{t+1}, i.e.,

$\nu_i^{t+1} = \nu_i^t - \beta_i^t (D_i x^{t+1} - w_i^{t+1})$ for all *i*

$\rho^{t+1} = \rho^t - \mu^t (Ax^{t+1} - y)$

Choose $\beta_i^{t+1} \geq \beta_i^t$ and $\mu^{t+1} \geq \mu^t$

End Do

Acknowledgements

This work was partially supported by the Federal Ministry of Education and Research (BMBF) in Germany under grant no. 03FH038I3 (MOSES).

References

Adler A and Guardo R 1996 Electrical impedance tomography: Regularized imaging and contrast detection *IEEE Trans. Biomed. Eng.* 15 170-9

Baraniuk R G and Jones D L 1994 A signal-dependent time-frequency representation: Fast algorithm for optimal kernel design *IEEE Trans. Signal Processing* 42(1) 134ï 46

Baraniuk R G 1999 *Optimal tree approximation with wavelets*: *Proc. SPIE 3813 Wavelet Applications in Signal and Image Processing VII*, Denver, 196 (October 26, 1999)

Baraniuk R G, DeVore R A, Kyriazis G and Yu X M 2002 Near best tree approximation, *Adv. Comput. Math.* 16(4) 357ï 73

Baraniuk R G 2007 Compressive sensing *IEEE Signal Processing Mag.*, 24(4) 118ï 120, 124

Baraniuk R G 2010 Model-based compressive sensing *IEEE Trans. Inf. Theory* 56 1982-2001

Barber D C and Brown B H 1998 Errors in reconstruction of resistivity images using a linear reconstruction technique *Physiol. Meas.* 9 101ï 4

Blue R S, Isaacson D and Newell J C 2000 Real-time three-dimensional electrical impedance imaging *Physiol. Meas.* 21 1-12

Borsic A, Graham B M, Adler A and Lionheart W R B 2010 In vivo impedance imaging with total variation regularization *IEEE Trans. Med. Imaging* 29(1) 44-54

Candès E J and Tao T 2005 Decoding by linear programming, *IEEE Trans. Inf. Theory*, 51(12) 4203-15

Cheney M, Isaacson D, Newell J C, Simske S and Goble J 1990 NOSER: an algorithm for solving the inverse conductivity problem *Int. J. Imaging Syst. Technol.* 2 66ï 75

Cheney M, Isaacson D and Newell J C 1999 Electrical impedance tomography *SIAM Rev.* 41 85ï 101

Dobson D C and Santosa F 1994 An image enhancement technique for electrical impedance tomography *Inverse Problems* 10 317ï 34

Donoho D L 2006 Compressed sensing *IEEE Trans. Info. Theory*, 52(4) 1289ï 306

Electrical impedance tomography and diffuse optical tomography reconstruction (EIDORS) website, http://eidors3d.sourceforge.net

Figueiredo M, Nowak R and Wright S 2007 Gradient projection for sparse reconstruction: application to compressed sensing and other inverse problems *IEEE Journal of selected topics in signal processing* 1 586-98

Gehre M, Kluth T, Lipponen A, Jin B, Seppanen A, Kaipio J and Maass P 2012 Sparsity reconstruction in electrical impedance tomography: an experimental evaluation. *J. Comput. Appl. Math.* 236 2126-36.

Gobel J C, Cheney M and Isaacson D 1992 Electrical Impedance Tomography in three dimensions *Appl. Comput. Electromagn. Soc. J.* 7 128-47

Goharian M, Soleimani M and Moran G 2009 A trust region subproblem for 3D electrical impedance tomography inverse problem using experimental data. *Prog. Electromagn. Res. Pier* 94 19-32

Gradient Projection for Sparse Reconstruction (GPSR) website, http://www.lx.it.pt/~mtf/GPSR/

Graham B M and Adler A 2006 A nodal Jacobian inverse solver for reduced complexity EIT reconstructions *Int. J. Inform. Syst. Sci.* 2 453ï 68

Graham B M and Adler A 2007 Electrode placement configurations for 3D EIT *Physiol. Meas.* 28 29ï 44

Halter R J, Hartov A and Paulsen K D 2007 Experimental justification for using 3D conductivity reconstructions in electrical impedance tomography, *Physiol. Meas.* 28 115ï 27

Holder D S (ed) 2005 *Electrical Impedance Tomography, Methods, History and Applications* (Bristol: Institute of Physics Publishing)

Javaherian A, Movafeghi A and Faghihi R 2013 Reducing negative effects of quadratic norm regularization on image reconstruction in electrical impedance tomography *Appl. Math. Model.* 37 5637ï 52

Javaherian A and Soleimani M 2013 Compressed sampling for boundary measurements in three-dimensional electrical impedance tomography, *Physiol. Meas.* 34 1133-50

Jin B, Khan T and Maass P 2012 A reconstruction algorithm for electrical impedance tomography based on sparsity regularization *Int. J. Numer. Meth. Eng.* 89(3) 337-53

Li C 2009 *An efficient algorithm for total variation regularization with applications to the single pixel camera and compressive sensing*, M.A. Thesis, Rice University, Houston, Texas

Lionheart W R B 2004 EIT reconstruction algorithms: pitfalls, challenges and recent developments *Physiol. Meas.* 25 125ï 42

Metherall P, Barber D C, Smallwood R H and Brown B H 1996 Three dimensional electrical impedance tomography *Nature* 380 509-12

Model-based Compressive Sensing Toolbox v1.1, http://dsp.rice.edu/software/model-based-compressive-sensing-toolbox-v11

Paulsen K, Meaney P, Moskowitz M and Sullivan J 1995 A dual mesh scheme for finite element based reconstruction algorithms *IEEE Trans. Med. Imaging* 14 504-14

Polydorides N, Lionheart W R B and McCann H 2002 Krylov subspace techniques: on the detection of brain activity with electrical impedance tomography *IEEE Trans. Med. Imaging* 21 596-603

Rauhut H 2010 Compressive sensing and structured random matrices, *In. Theoretical foundations and numerical methods for sparse recovery* De Gruyter, volume 9 of Radon Series Comp. Appl. Math. p.p. 1ï 92

Seo J K, Lee J, Kim S W, Zribi H and Woo E J 2008 Frequency-difference electrical impedance tomography (fdEIT): algorithm development and feasibility study *Physiol. Meas.* 29 929ï 44

Shewchuk J R 1994 *An introduction to the conjugate gradient method without the agonizing pain* School of Computer Science, Carnegie Mellon University, Pittsburgh, PA, USA

Sparse Reconstruction by Separable Approximation (SpaRSA) website, http://www.lx.it.pt/~mtf/SpaRSA

TV minimization by Augmented Lagrangian and Alternating direction Algorithms (TVAL3) website, http://www.caam.rice.edu/~optimization/L1/TVAL3

Vauhkonen P J, Vauhkonen M, Savolainen T and Kaipio J P 1999 Three dimensional electrical impedance tomography based on the complete electrode model *IEEE Trans. Biomed. Eng.* 46 1150-60

Wright S, Nowak R and Figueiredo M 2009 Sparse reconstruction by separable approximation, *IEEE Trans. Signal Process.* 57 2479ï 93

Yang C L, Wei H Y, Adler A and Soleimani M 2013 Reducing computational costs in large scale 3D EIT by using a sparse Jacobian matrix with block-wise CGLS reconstruction *Physiol. Meas.* 34 645ï 58

Yorkey T J, Webster J G and Tompkins W J 1987 Comparing reconstruction algorithms for electrical impedance tomography *IEEE Trans. Biomed. Eng.* 34 843ï 52